Computational Aspects of Elasto-Plastic Deformation in Polycrystalline Solids

Ronaldo I. Borja
e-mail: borja@stanford.edu

Helia Rahmani

Department of Civil and Environmental Engineering, Stanford University, Stanford, CA 94305

The overall elasto-plastic behavior of single crystals is governed by individual slips on crystallographic planes, which occur when the resolved shear stress on a critical slip system reaches a certain maximum value. The challenge lies in identifying the activated slip systems for a given load increment since the process involves selection from a pool of linearly dependent slip systems. In this paper, we use an "ultimate algorithm" for the numerical integration of the elasto-plastic constitutive equation for single crystals. The term ultimate indicates exact integration of the elasto-plastic constitutive equation and explicit tracking of the sequence of slip system activation. We implement the algorithm into a finite element code and report the performance for polycrystals subjected to complicated loading paths including non-proportional and reverse/cyclic loading at different crystal orientations. It is shown that the ultimate algorithm is comparable to the widely used radial return algorithm for J_2 plasticity in terms of global numerical stability. [DOI: 10.1115/1.4005898]

1 Introduction

Many engineered and natural materials possess crystalline microstructures with well defined slip planes and glide directions. Plastic deformations in these materials arise when the resolved shear stress triggers slip on some of the available systems. Plastic flow according to the maximum resolved shear stress criterion is particularly important near the crack tip as it impacts the direction of crack growth [1,2]. Irrespective of whether yielding is large-scale or small-scale/asymptotic near a crack tip [3], the challenge lies in identifying the slip systems activated by a given load increment since the process usually involves selection from a pool of linearly dependent systems.

Single crystals may be considered as building blocks revealing relevant features of the atomic structure of a given solid. Most natural and engineered materials, including metals and igneous rocks, have polycrystalline microstructures. Each grain is a single crystal that could be oriented in a random manner, resulting in overall component properties that can deviate from being one-directional. Crystal sizes range from nanometer-scale to centimeter-scale, or from a few atomic layers to millions of them. Experimentally, it is possible to determine the crystal microstructure by diffraction to allow some deterministic properties to be included in constitutive modeling. Constitutive equations for elasto-plastic behavior of single crystals were first formulated for continuum mechanics by Mandel [4], Hill [5], and Maier [6], and extended to finite deformations by Rice [7], Hill and Rice [8], Asaro and Rice [9], and others. However, although crystal plasticity theory has been well developed for many years, robust stress-point integration algorithms for the theory remain scarce. Many of the crystal plasticity algorithms are non-convergent for some loading paths, hampering efforts to implement them into multipurpose finite element codes.

One of the first models to use polycrystalline representation for the yielding of metals was proposed by Bishop and Hill [10,11]. They neglected the contribution of the elastic strains and did not discuss the sequence of activation of slip systems in the crystal. Lin [12] considered the elastic strains, but made a critical assumption that the elastic and plastic strains were the same for each crystal. Hutchinson [13] and Budiansky and Wu's [14] formulations accounted for all twelve slip systems in face centered cubic (f.c.c.) crystals but employed a trial and error procedure to determine the active slip systems. Iwakuma and Nemat-Nasser [15] and Peirce et al. [16] studied the formation of shear bands in crystals, although their work was restricted to two slip systems in each crystal. Predicting the active systems of f.c.c. crystals in multislip orientations had been the object of studies by Kocks [17], Kocks and Canova [18], and Havner [19], among others.

The integration algorithm for a single crystal utilizes the slip rates as the primary unknowns. In principle, determining the slip rates is trivial if the independent active slip systems are known. Koiter's [20] uniqueness and variational theorems for elasto-plastic materials with a singular yield surface provide a means for determining these slip rates. A seemingly attractive numerical algorithm for determining the active systems is based on return mapping for rate-independent multisurface plasticity advocated by Simo et al. [21]. In this algorithm, a trial elastic stress predictor is calculated, and if yielding is detected a plastic corrector is introduced by "returning" the predictor stress iteratively to the active yield surface(s). While this algorithm may work for linearly independent multisurface plasticity models, it could suffer from lack of local convergence when the systems include redundant constraints [22].

Rate-dependent regularization is often employed to circumvent the problem of redundant constraints. For example, Cuitiño and Ortiz [23] and Steinmann and Stein [24] used a viscoplastic formulation where redundant constraints do not occur because of the rate-dependent regularization. There may be some physical justification for this approach since it is known that plastic flow due to dislocation motion is inherently rate-dependent [25,26]. In the rate-dependent formulation, the slip rates are directly related to the instantaneous resolved shear stresses: there is no yield surface, there are no loading/unloading criteria, and there is no need to distinguish between active and inactive slip systems. However, when the rate sensitivity is small the resolved shear stress on a system cannot exceed a given slip resistance. It is this latter condition that renders the rate-dependent formulation very difficult to solve [27]: when the resolved shear stress is slightly higher than the strength,

Manuscript received July 26, 2011; final manuscript received November 10, 2011; accepted manuscript posted February 13, 2012; published online April 6, 2012. Assoc. Editor: Huajian Gao.

the set of constitutive equations becomes exceedingly stiff and gives rise to unrealistic values of slip rates [28].

There have been a number of algorithms proposed in the literature that also work well for rate-independent crystal models. They include the ultimate algorithm by Borja and Wren [22], the generalized inverse approaches by Anand and Kothari [29] and Schröder and Miehe [30], and the diagonal shift method by Miehe and Schröder [31]. A common idea among these methods is the formulation of a local coefficient matrix to solve the plastic slips in the active systems and inspection of the singularity of this matrix to eliminate the redundant constraints. Whereas no universally accepted solution exists as to how to identify a unique set of active systems in the rate-independent limit [32], we focus on the ultimate algorithm advocated in Ref. [22] because of the following attributes of the method: (a) it is exact for Taylor hardening crystals, (b) it is unconditionally convergent on the local level since it does not employ a local iteration, and (c) it exhibits a global numerical stability comparable to that of the widely used radial return algorithm for J_2 plasticity.

By "exact" integration we mean that for a given strain increment applied as a ramp function the algorithm produces the exact local final stress irrespective of the size of the strain increment. As a point of comparison, we recall that the radial return algorithm proposed by Wilkins [33] for J_2 plasticity is exact only for radial loading. Exact integration independent of the step size is realized by following the sequence of slip system activation. We remark that there is no guarantee that a previously active system will remain active when other systems activate, even if the strain increment is applied as a ramp function, so it is important to follow the sequence of activation/deactivation within the increment. This is particularly true when using the algorithm, for example, to calculate the stresses near a crack tip where the strain increment is expected to be very large.

The contribution of this paper lies in the implementation of the ultimate algorithm into a multipurpose nonlinear finite element code with the goal of assessing its performance for the simulation of 3D boundary-value problems in solid mechanics. We limit the scope of this paper to infinitesimal deformation and Taylor hardening with a constant plastic modulus. The gold test for assessing the performance of the algorithm is how well it compares with the widely used radial return algorithm for J_2 plasticity with respect to numerical stability [34], since the latter model is simply the "smeared" version of the crystal plasticity model. Remarkably, the ultimate algorithm is shown to be just as stable as the radial return algorithm. Numerical examples include complex loading paths, non-proportional loading, and reverse/cyclic loading in 3D.

2 Crystal Plasticity Theory

We denote by $\dot{\boldsymbol{\epsilon}}$ the homogeneous strain rate in a crystal, which is composed of elastic and plastic parts,

$$\dot{\boldsymbol{\epsilon}} = \dot{\boldsymbol{\epsilon}}^{\mathrm{e}} + \dot{\boldsymbol{\epsilon}}^{\mathrm{p}} \tag{1}$$

The plastic component $\dot{\boldsymbol{\epsilon}}^{\mathrm{p}}$ arises from slips on crystallographic planes. We denote by $\boldsymbol{n}^{(\beta)}$ the unit normal to a crystallographic plane containing the β-slip system and by $\boldsymbol{m}^{(\beta)}$ the corresponding direction of plastic slip. If $\dot{\gamma}^{(\beta)}$ is the plastic slip rate, then a point on the slip plane with position vector $\boldsymbol{x}$ will move at a velocity

$$\boldsymbol{v}^{(\beta)} = \dot{\gamma}^{(\beta)}(\boldsymbol{x}\cdot\boldsymbol{n}^{(\beta)})\boldsymbol{m}^{(\beta)} \tag{2}$$

The velocity gradient contributed by glide strain β can be evaluated from the expression

$$\nabla\boldsymbol{v}^{(\beta)} = \dot{\gamma}^{(\beta)}\boldsymbol{m}^{(\beta)}\otimes\boldsymbol{n}^{(\beta)} \tag{3}$$

where $\boldsymbol{m}^{(\beta)}\otimes\boldsymbol{n}^{(\beta)}$ is the slip tensor. This form for the slip tensor is analogous to that produced in strong discontinuity kinematics [35–37]. Summing over all active crystallographic slips results in the following expression for the plastic strain rate:

$$\dot{\boldsymbol{\epsilon}}^{\mathrm{p}} = \sum_{\beta\text{ active}} \dot{\gamma}^{(\beta)}\boldsymbol{\alpha}^{(\beta)} \tag{4}$$

where

$$\boldsymbol{\alpha}^{(\beta)} = \frac{1}{2}(\boldsymbol{m}^{(\beta)}\otimes\boldsymbol{n}^{(\beta)} + \boldsymbol{n}^{(\beta)}\otimes\boldsymbol{m}^{(\beta)}) \tag{5}$$

Note that $\mathrm{tr}(\boldsymbol{\alpha}^{(\beta)}) = \boldsymbol{m}^{(\beta)}\cdot\boldsymbol{n}^{(\beta)} = 0$, so the overall deformation is volume-preserving. Figure 1 shows the kinematics of crystal slips.

We denote the overall crystal stress by $\boldsymbol{\sigma}$. The elastic rate constitutive equation for the crystal takes the form

$$\dot{\boldsymbol{\sigma}} = \boldsymbol{c}^{\mathrm{e}} : \left(\dot{\boldsymbol{\epsilon}}^{\mathrm{e}} - \sum_{\beta\text{ active}} \dot{\gamma}^{(\beta)}\boldsymbol{\alpha}^{(\beta)}\right) \tag{6}$$

where $\boldsymbol{c}^{\mathrm{e}}$ is the elasticity tensor. The problem lies in identifying the active slip systems.

Consider a crystal with $2N$ potentially active slip systems, which include both "forward" and "reverse" slips. For f.c.c. crystals $N=12$, let $\tau_Y^{(\beta)}$ represent the yield stress for each slip system. The system is potentially active if at least one of the following conditions is satisfied:

$$f^{(\beta)} = \begin{cases} \boldsymbol{\sigma}:\boldsymbol{\alpha}^{(\beta)} - \tau_Y^{(\beta)} = 0, & \beta = 1, 2, \ldots, N \\ -\boldsymbol{\sigma}:\boldsymbol{\alpha}^{(\beta)} - \tau_Y^{(\beta)} = 0, & \beta = N+1, N+2, \ldots, 2N \end{cases} \tag{7}$$

The above yield conditions represent $2N$ hyperplanes in the general stress space defining boundaries of the elastic region. The plastic strain rate can be written in Koiter's form [20] as

$$\dot{\boldsymbol{\epsilon}}^{\mathrm{p}} = \sum_{\beta=1}^{2N} \dot{\gamma}^{(\beta)}\frac{\partial f^{(\beta)}}{\partial\boldsymbol{\sigma}} = \sum_{\beta=1}^{2N}\dot{\gamma}^{(\beta)}\boldsymbol{\alpha}^{(\beta)} \tag{8}$$

where $\boldsymbol{\alpha}^{(\beta)} = -\boldsymbol{\alpha}^{(\beta-N)}$ for $N<\beta\le 2N$. The slip rates $\dot{\gamma}^{(\beta)}$ satisfy the classical Kuhn-Tucker conditions [14]

$$\dot{\gamma}^{(\beta)} \ge 0, \quad f^{(\beta)} \le 0, \quad \dot{\gamma}^{(\beta)}f^{(\beta)} = 0 \tag{9}$$

for all β.

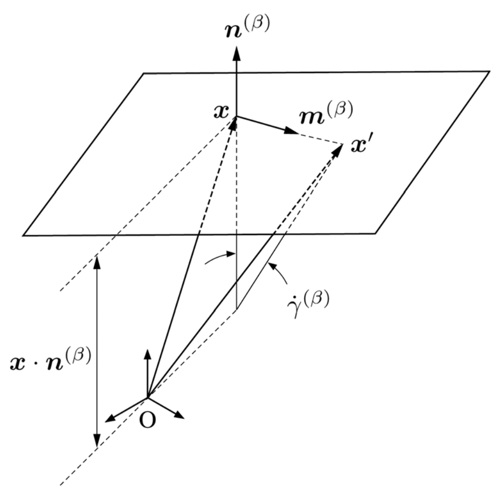

Fig. 1 Kinematics of crystal slips

To complete the constitutive theory, we assume the Taylor hardening law [38]

$$\dot{\tau}_Y^{(\beta)} = h \sum_{\xi=1}^{2N} \dot{\gamma}^{(\xi)} \tag{10}$$

According to the above equation, plastic slip rates generate an equal increment of hardening and result in the elastic region expanding uniformly. There is only one required plastic modulus, namely, h, making it a simple hardening law for crystal plasticity. Since forward and reverse slips generate the same rate of hardening, we can write Eq. (7) in the more concise form

$$f^{(\beta)} = |\boldsymbol{\sigma} : \boldsymbol{\alpha}^{(\beta)}| - \tau_Y^{(\beta)} = 0, \quad \beta = 1, 2, \ldots N \tag{11}$$

The hardening law then simplifies to

$$\dot{\tau}_Y^{(\beta)} = h \sum_{\xi=1}^{N} \dot{\gamma}^{(\xi)} \tag{12}$$

3 Identification of Active Slip Systems

Consider finite slip increments $\Delta\gamma^{(\beta)}$ for all possible slip systems β. We define the set of slip systems

$$\mathcal{J}_{\text{act}} = \{\beta \in \{1, 2, \ldots, N\} \mid f^{(\beta)} = 0 \text{ and } \Delta\gamma^{(\beta)} \geq 0\} \tag{13}$$

The slip systems are linearly independent if

$$\sum_{\beta \in \overline{\mathcal{J}}_{\text{act}}} \Delta\gamma^{(\beta)} \boldsymbol{\alpha}^{(\beta)} = \mathbf{0} \quad \Rightarrow \quad \Delta\gamma^{(\beta)} = 0 \quad \forall \beta \in \overline{\mathcal{J}}_{\text{act}} \tag{14}$$

where $\overline{\mathcal{J}}_{\text{act}} \subset \mathcal{J}_{\text{act}}$ is the set of linearly independent active constraints [39]. It follows that $\mathcal{J}_{\text{act}} \backslash \overline{\mathcal{J}}_{\text{act}}$ is the set of redundant constraints. We see that the tensors $\boldsymbol{\alpha}^{(\beta)}$ for $\beta \in \overline{\mathcal{J}}_{\text{act}}$ form linearly independent bases for the incremental plastic strain tensor $\Delta\boldsymbol{\epsilon}^{\text{p}}$. Note that $\Delta\boldsymbol{\epsilon}^{\text{p}}$ is a symmetric tensor, so it can only have six independent elements. Furthermore, $\text{tr}(\Delta\boldsymbol{\epsilon}^{\text{p}}) = 0$, so $\overline{\mathcal{J}}_{\text{act}}$ can have no more than five elements.

The basic idea behind the ultimate algorithm is to determine the plastic strain increment $\Delta\boldsymbol{\epsilon}^{\text{p}}$ as a function of the imposed strain increment $\Delta\boldsymbol{\epsilon}$, assuming the latter is applied proportionally in the sense of the ramp function

$$\Delta\boldsymbol{\epsilon}(\tau) = \kappa\Delta\boldsymbol{\epsilon}, \qquad \kappa = \tau/\Delta t \tag{15}$$

where $0 \leq \tau \leq \Delta t$. As usual, we write Eq. (1) in discrete form as

$$\Delta\boldsymbol{\epsilon} = \Delta\boldsymbol{\epsilon}^{\text{e}} + \Delta\boldsymbol{\epsilon}^{\text{p}} \tag{16}$$

A systematic procedure exists for identifying the active slip systems in a crystal subjected to proportional deformation [22]. We begin by assuming that $|\boldsymbol{\alpha}^{(\beta)} : \boldsymbol{\sigma}_n| - \tau_{Y,n} < 0$ for all slip systems so that the stress point initially lies within the elastic region. An imposed deformation $\kappa\Delta\boldsymbol{\epsilon}$ given by Eq. (15) applied to the crystal will produce the stress evolution

$$\boldsymbol{\sigma}(t) = \boldsymbol{\sigma}_n + \int_0^{\kappa\Delta t} \boldsymbol{c}^{\text{e}} : \dot{\boldsymbol{\epsilon}}\, \mathrm{d}\tau = \boldsymbol{\sigma}_n + \kappa\boldsymbol{c}^{\text{e}} : \Delta\boldsymbol{\epsilon} \tag{17}$$

We evaluate κ for each slip system and construct a set

$$\Psi_1 = \left\{\kappa^{(\beta)} \in R_+ \middle| \psi^{(\beta)}\boldsymbol{\alpha}^{(\beta)} : \boldsymbol{\sigma}(t) - \tau_{Y,n} = 0\right\} \tag{18}$$

where $\psi^{(\beta)} = \text{sign}(\boldsymbol{\alpha}^{(\beta)} : \boldsymbol{\sigma}(t))$. It is obvious that if $\kappa^{(\beta)} > 1$ for all β, then the process remains elastic for the given strain increment. However, if $\kappa^{(\beta)} < 1$ for some $\beta \in \{1, 2, \ldots, N\}$, then an initial operative (primary) slip system must have been activated during this strain increment. This slip system is the constraint β_1 that yields the smallest value of $\kappa^{(\beta)}$.

Next, we consider the activation of a duplex system (two active constraints). To identify the secondary slip system, we first assume that we have an active primary slip system β_1 for our initial condition. We then apply the ray of deformation $\kappa\Delta\boldsymbol{\epsilon}$ and search for the secondary slip system. During this search the evolution of the crystal stress is given by the equation

$$\begin{aligned}\boldsymbol{\sigma}(t) &= \boldsymbol{\sigma}_n + \int_0^{\kappa\Delta t} \boldsymbol{c}^{\text{e}} : (\dot{\boldsymbol{\epsilon}} - \dot{\boldsymbol{\epsilon}}^{\text{p}})\, \mathrm{d}t \\ &= \boldsymbol{\sigma}_n + \boldsymbol{c}^{\text{e}} : (\kappa\Delta\boldsymbol{\epsilon} - \Delta\gamma^{(\beta_1)}\psi^{(\beta_1)}\boldsymbol{\alpha}^{(\beta_1)})\end{aligned} \tag{19}$$

Here we assume that the primary slip system β_1 continues to be active during the search process. Thus, for a constant plastic modulus h, the stress must satisfy the consistency condition

$$\psi^{(\beta_1)}\boldsymbol{\alpha}^{(\beta_1)} : \boldsymbol{\sigma}(t) - (\tau_{Y,n} + h\Delta\gamma^{(\beta_1)}) = 0 \tag{20}$$

which gives the incremental slip on the primary system

$$\Delta\gamma^{(\beta_1)} = \frac{\psi^{(\beta_1)}\boldsymbol{\alpha}^{(\beta_1)} : \boldsymbol{c}^{\text{e}}}{\mu_{\text{c}} + h} : \kappa\Delta\boldsymbol{\epsilon} \tag{21}$$

where μ_{c} is the crystal elastic shear modulus. Substituting this incremental slip into Eq. (19) yields the following alternative form for the evolution of the crystal stress during the search for the secondary slip system

$$\boldsymbol{\sigma}(t) = \boldsymbol{\sigma}_{c,n} + \kappa\boldsymbol{c}^{\text{ep}} : \Delta\boldsymbol{\epsilon} \tag{22}$$

where

$$\boldsymbol{c}^{\text{ep}} = \boldsymbol{c}^{\text{e}} - \frac{1}{\mu_{\text{c}} + h}\boldsymbol{c}^{\text{e}} : \boldsymbol{\alpha}^{(\beta_1)} \otimes \boldsymbol{\alpha}^{(\beta_1)} : \boldsymbol{c}^{\text{e}} \tag{23}$$

is the elasto-plastic tangent tensor. We can again evaluate $\kappa^{(\beta)}$ for each slip system and construct the set

$$\Psi_2 = \left\{\kappa^{(\beta)} \in R_+ \middle| \psi^{(\beta)}\boldsymbol{\alpha}^{(\beta)} : \boldsymbol{\sigma}(t) - (\tau_{Y,n} + h\Delta\gamma^{(\beta_1)}) = 0\right\} \tag{24}$$

If $\kappa^{(\beta)} < 1$ for some $\beta \in \{1, 2, \ldots, N\} \backslash \beta_1$, then the secondary slip system must be the constraint β_2 that yields the smallest value of $\kappa^{(\beta)}$.

The preceding ideas can be extended to multislip processes. We assume that a given strain increment simultaneously activates $m \leq 4$ linearly independent slip systems $\beta_1, \ldots, \beta_m$, and we want to identify the $(m+1)$st active system. For the ray of deformation $\kappa\Delta\boldsymbol{\epsilon}$ the evolution of the crystal stress is given by the equation

$$\boldsymbol{\sigma}(t) = \boldsymbol{\sigma}_n + \boldsymbol{c}^{\text{e}} : \left(\kappa\Delta\boldsymbol{\epsilon} - \sum_{i=1}^{m} \Delta\gamma^{(\beta_i)}\psi^{(\beta_i)}\boldsymbol{\alpha}^{(\beta_i)}\right) \tag{25}$$

The slips are then determined from imposing a total of m independent consistency conditions,

$$\psi^{(\beta_i)}\boldsymbol{\alpha}^{(\beta_i)} : \boldsymbol{\sigma}(t) - \left(\tau_{Y,n} + h\sum_{i=1}^{m} \Delta\gamma^{(\beta_i)}\right) = 0, \qquad i = 1, \ldots, m \tag{26}$$

which gives

$$\Delta\gamma^{(\beta_i)} = \kappa \sum_{j=1}^{m} g_{ij}^{-1}\psi^{(\beta_j)}\boldsymbol{\alpha}^{(\beta_j)} : \boldsymbol{c}^{\text{e}} : \Delta\boldsymbol{\epsilon} \tag{27}$$

Step 1. Compute $\boldsymbol{\sigma}_{n+1}^{\mathrm{tr}} = \boldsymbol{\sigma}_n + \boldsymbol{c}^{\mathrm{e}} : \Delta\boldsymbol{\epsilon}$
Assemble $\mathcal{J}^{\mathrm{tr}} = \{\beta \mid \psi^{(\beta)}\boldsymbol{\alpha}^{(\beta)} : \boldsymbol{\sigma}_{n+1}^{\mathrm{tr}} - \tau_{Y,n} > 0\}$
Step 2. Check: $\mathcal{J}^{\mathrm{tr}} = \varnothing$?
Yes, elastic response: set $\boldsymbol{\sigma}_{n+1} = \boldsymbol{\sigma}_{n+1}^{\mathrm{tr}}$, $\tau_{Y,n+1} = \tau_{Y,n}$, $\boldsymbol{c} = \boldsymbol{c}^{\mathrm{e}}$, and exit.
Step 3. No, plastic response: set $\mathcal{J}_{\mathrm{act}} = \{\beta \mid \psi^{(\beta)}\boldsymbol{\alpha}^{(\beta)} : \boldsymbol{\sigma}_n - \tau_{Y,n} = 0\}$ and call Box 2
Step 4. Update $\boldsymbol{\sigma}_{n+1} = \boldsymbol{\sigma}_n$, $\tau_{Y,n+1} = \tau_{Y,n}$, $\boldsymbol{c} = \boldsymbol{c}^{\mathrm{ep}}$, and exit.

Box 1 Predictor phase for crystal plasticity calculations

where

$$g_{ij} = \psi^{(\beta_i)}\psi^{(\beta_j)}\boldsymbol{\alpha}^{(\beta_i)} : \boldsymbol{c}^{\mathrm{e}} : \boldsymbol{\alpha}^{(\beta_j)} + h \tag{28}$$

and $\det(g_{ij}) > 0$ from the assumption of linear independence of the active slip systems. Note that since $\mathrm{tr}(\boldsymbol{\alpha}) = 0$ and $\boldsymbol{\alpha}^{(\beta)} : \boldsymbol{\alpha}^{(\beta)} = 1/2$, we have

$$g_{ij} = \begin{cases} \mu_{\mathrm{c}} + h, & \text{if } i = j \\ 2\mu_{\mathrm{c}}\psi^{(\beta_i)}\psi^{(\beta_j)}\boldsymbol{\alpha}^{(\beta_i)} : \boldsymbol{\alpha}^{(\beta_j)} + h, & \text{otherwise} \end{cases} \tag{29}$$

Equivalently, the evolution of the crystal stress $\boldsymbol{\sigma}(t)$ can be evaluated from Eq. (22) with the elasto-plastic tangent tensor obtained from the expression

$$\boldsymbol{c}^{\mathrm{ep}} = \boldsymbol{c}^{\mathrm{e}} - \sum_{i=1}^{m}\sum_{j=1}^{m} \psi^{(\beta_i)}\psi^{(\beta_j)} g_{ij}^{-1} \boldsymbol{c}^{\mathrm{e}} : \boldsymbol{\alpha}^{(\beta_i)} \otimes \boldsymbol{\alpha}^{(\beta_j)} : \boldsymbol{c}^{\mathrm{e}} \tag{30}$$

We can then evaluate $\kappa^{(\beta)}$ for each slip system and construct the set

$$\Psi_{m+1} = \left\{ \kappa^{(\beta)} \in R_+ \middle| \psi^{(\beta)}\boldsymbol{\alpha}^{(\beta)} : \boldsymbol{\sigma}(t) - \left(\tau_{Y,n} + \kappa^{(\beta)} \sum_{j=1}^{m} g_{ij}^{-1} \psi^{(\beta_j)} \boldsymbol{\alpha}^{(\beta_j)} : \boldsymbol{c}^{\mathrm{e}} : \Delta\boldsymbol{\epsilon} \right) \right\} \tag{31}$$

as before. If $\kappa^{(\beta)} < 1$ for some $\beta \in \{1, 2, \ldots, N\} \backslash \{\beta_1, \ldots, \beta_m\}$, then the next active slip system β_{m+1} corresponds to the smallest element of Ψ_{m+1}. Note that the elasto-plastic moduli tensor $\boldsymbol{c}^{\mathrm{ep}}$ changes each time a new slip system is added or removed from the set $\overline{\mathcal{J}}_{\mathrm{act}}$.

4 Ultimate Algorithm

The goal of the stress-point algorithm is to integrate the crystal stress and construct the crystal stress-strain matrix for a given initial stress state and crystal strain increment. In the process, the algorithm identifies the independent slip systems without local iteration, so the method is unconditionally convergent at the stress-point level. Furthermore, for a constant plastic modulus the algorithmic tangent tensor approaches a constant continuum moduli tensor once the global solution finds the set of independent active constraints. Thus, the global Newton iteration is superconvergent in the sense that the error will drop to zero once the independent active constraints have been identified.

At the stress-point level there are two groups of input parameters identifying the properties of a crystal. The first group describes the mechanical properties of the crystal and includes Young's modulus E and Poisson's ratio ν (used to calculate the elastic stiffness matrix), and the initial yield strength τ_{Y0} and hardening parameter h (used to define the yield function and its evolution). These four parameters are stored in real scalar variables. The second group defines the geometric properties of the crystal and consists of the potential slip systems. Each slip system is identified by two vectors containing components of the slip direction $\boldsymbol{m}^{(\beta)}$ and normal vector $\boldsymbol{n}^{(\beta)}$ to the crystallographic plane containing the slip direction. These two vectors depend on the type and orientation of the crystal. For example, f.c.c. crystals have a total of 24 slip systems. Slip directions and normal vectors are multiplied by a rotation matrix to account for the orientation of the crystal. The slip normals and slip directions are stored in an array of dimension $3 \times 3 \times n_{\mathrm{slip}}$, where n_{slip} is the number of slip systems. An additional scalar variable is used to store the value of the cumulative plastic slip at each stress point.

Boxes 1 and 2 show flow charts of the elastic predictor and "plastic corrector" phases of the algorithm. Strictly speaking, the

Step 1. If $\mathcal{J}_{\mathrm{act}} = \varnothing$, set $\boldsymbol{c} = \boldsymbol{c}^{\mathrm{e}}$ and go to Step 6
Step 2. Select $\overline{\mathcal{J}}_{\mathrm{act}} \subset \mathcal{J}_{\mathrm{act}}$
Step 3. Compute $\Delta\tilde{\gamma}^{(\beta)}$ for all $\beta \in \overline{\mathcal{J}}_{\mathrm{act}}$
Step 4. If $\Delta\tilde{\gamma}^{(\beta)} < 0$, drop $\Delta\tilde{\gamma}_{\min}^{(\beta)}$ from $\overline{\mathcal{J}}_{\mathrm{act}}$ and go to Step 3
Step 5. Compute $\boldsymbol{c} = \boldsymbol{c}^{\mathrm{ep}}$ for the current $\overline{\mathcal{J}}_{\mathrm{act}}$
Step 6. Compute $\kappa^{(\beta)}$ for all $\beta \notin \overline{\mathcal{J}}_{\mathrm{act}}$ and assemble Ψ_{n+1}
Step 7. Set $\kappa^{(\beta_{m+1})} = \min(1, \min \Psi_{n+1})$ and update
$\boldsymbol{\sigma}_n \leftarrow \boldsymbol{\sigma}_n + \kappa^{(\beta_{m+1})}\boldsymbol{c}^{\mathrm{ep}} : \Delta\boldsymbol{\epsilon}$
$\tau_{Y,n} \leftarrow \tau_{Y,n} + \kappa^{(\beta_{m+1})} h \sum_{\beta \in \overline{\mathcal{J}}_{\mathrm{act}}} \Delta\tilde{\gamma}^{(\beta)}$
$\Delta\boldsymbol{\epsilon} \leftarrow \Delta\boldsymbol{\epsilon} - \kappa^{(\beta_{m+1})}\Delta\boldsymbol{\epsilon}$
$\overline{\mathcal{J}}_{\mathrm{act}} \leftarrow \overline{\mathcal{J}}_{\mathrm{act}} \cup \beta_{m+1}$
Step 8. If $\kappa^{(\beta_{m+1})} < 1$, go to Step 2.
Step 9. Return to Box 1.

Box 2 Plastic integrator based on the ultimate algorithm [9]

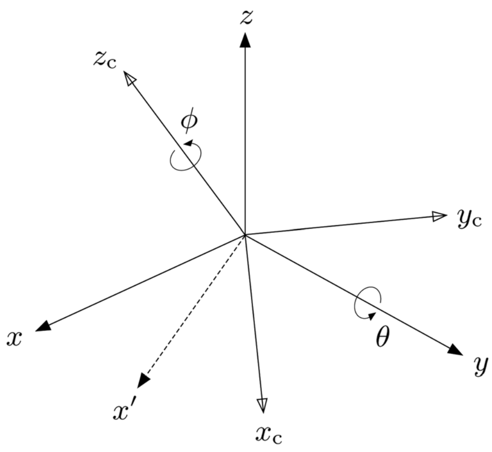

Fig. 2 Euler angles defining crystal axes (x_c, y_c, z_c) relative to the fixed system (*x, y, z*)

corrector phase does not correct the predictor phase since the trial stress predictor $\boldsymbol{\sigma}_{n+1}^{\text{tr}}$ is discarded once the algorithm detects some plasticity in the crystal (i.e., when $\mathcal{J}^{\text{tr}} \neq \emptyset$). Instead, the algorithm starts anew with the current stress $\boldsymbol{\sigma}_n$ and calls the ultimate algorithm summarized in Box 2 to systematically activate the relevant slip systems. Prior to calling Box 2, the predictor phase first identifies the hyperplanes on which the stress point now lies and collects them in the set $\mathcal{J}_{\text{act}}$. This set may also contain redundant constraints that are later filtered out in Box 2.

In Step 2 of Box 2, the linearly independent active constraints are identified from the set $\mathcal{J}_{\text{act}}$ and stored in the set $\overline{\mathcal{J}}_{\text{act}}$ as follows. First, the elements g_{ij} defined in Eq. (29) are assembled into an array accommodating all the constraints in $\mathcal{J}_{\text{act}}$. In the presence of redundant constraints, this array is singular; however, a simple *LDU* factorization automatically identifies the redundant constraints from the zero elements in *D*, which are then discarded. The same factorized matrix is used to solve the slips in the remaining independent active constraints from the equation

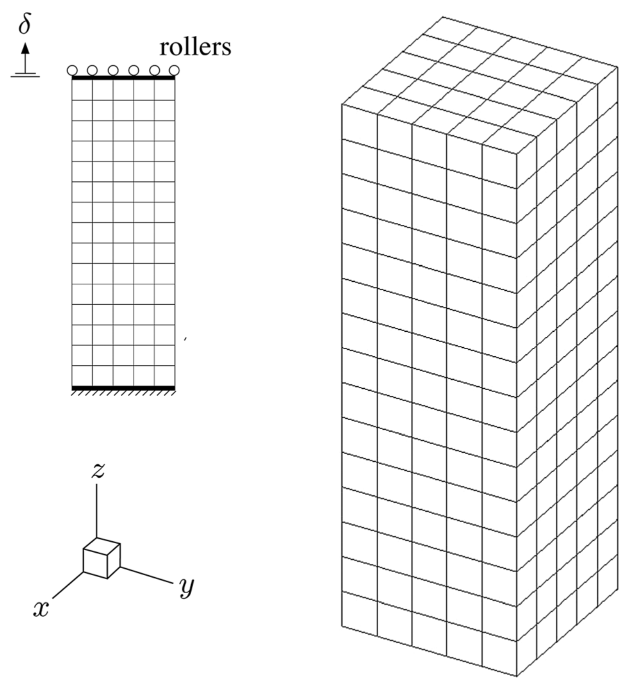

Fig. 3 Uniaxial loading of a cubical solid with a square cross section

Table 1 Euler angles for three different crystal orientations in a cubical solid

Orientation	θ, deg	ϕ, deg
1	45	22
2	20	0
3	0	0

$$\Delta\tilde{\gamma}^{(\beta_i)} = \sum_{j=1}^{m} g_{ij}^{-1} \psi^{(\beta_j)} \boldsymbol{\alpha}^{(\beta_j)} : \boldsymbol{c}^{\text{e}} : \Delta\boldsymbol{\epsilon} \tag{32}$$

As pointed out in the Introduction and in Ref. [9], there is no guarantee that an active slip system will remain active even if one applies a monotonic unidirectional incremental strain (i.e., a ramp function). In other words, as more slip systems activate it is possible that other previously active systems could unload. To account for this possibility, Step 4 of Box 2 identifies a deactivating system from the sign of the calculated slip. Once the algorithm detects that all of the incremental strain has been applied (i.e., $\kappa^{(\beta_{m+1})} = 1$), it returns to Box 1 with the final values of the crystal stress, yield stress, and the elastoplastic tangential moduli. These are stored in the updated $\boldsymbol{\sigma}_n$, $\tau_{Y,n}$, and $\boldsymbol{c}^{\text{ep}}$, respectively.

5 Numerical Simulations

In this section, we use the finite element method to solve a number of 3D boundary-value problems employing the proposed crystal plasticity algorithm.

In all the simulations, we assumed infinitesimal deformation so that the nonlinearity may be attributed solely to the material constitutive response. We use eight-node hexahedral finite elements with *B*-bar integration to circumvent mesh locking in the incompressible and nearly incompressible regimes. Newton's method is used for the global iterations, and different solid shapes are considered.

Because the structural response depends on crystal orientation, it is necessary to define the crystal orientations with respect to a fixed reference frame. In an f.c.c. crystal the eight $\{1\ 1\ 1\}$ octahedral planes in the crystal reference frame each contain three $\langle 110 \rangle$ slip directions that are 60 deg apart, for a total of 24 possible slip systems. Here we consider the (*x, y, z*)-system as our fixed

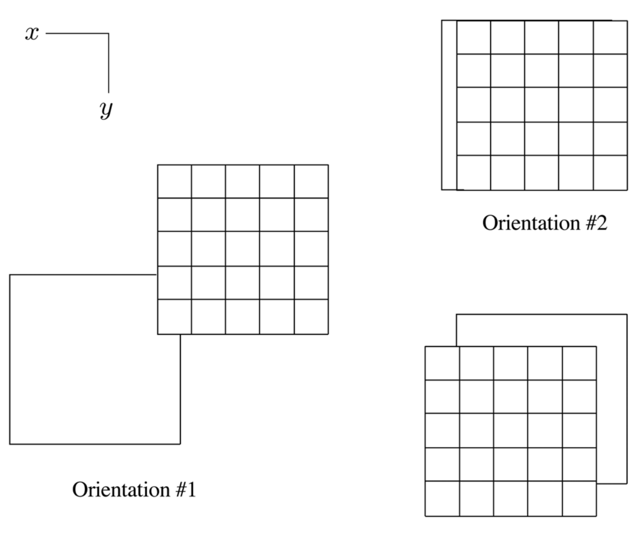

Fig. 4 Lateral movement of top end (cross-section with a mesh) relative to bottom end (cross-section without a mesh) at different crystal orientations. Displacements magnified 80 ×.

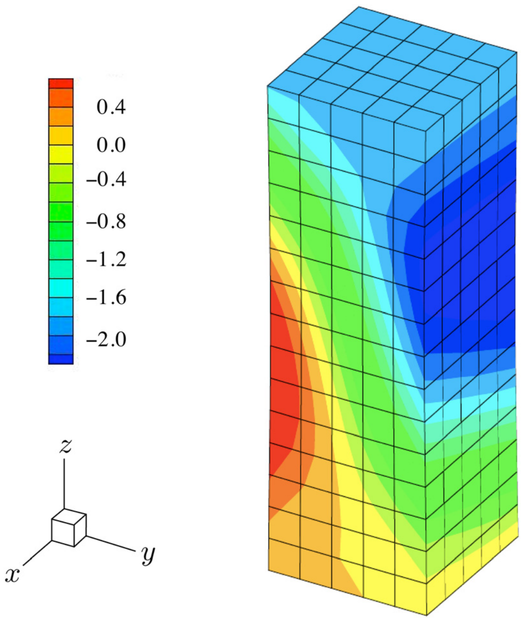

Fig. 5 Deformation band forming in the cubical sample for crystal orientation 1. Color bar is *y*-displacement in cm.

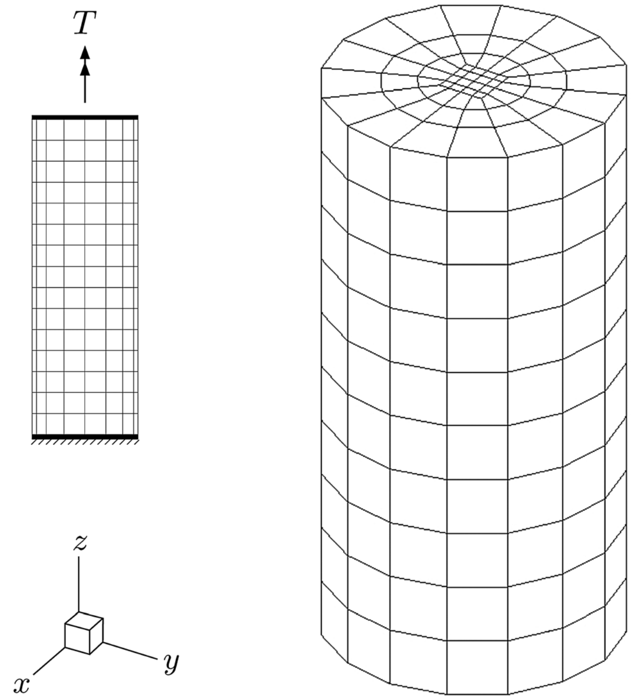

Fig. 6 Cyclic twisting of a cylindrical solid with a circular cross section

reference frame and the (x_c, y_c, z_c)-system as the crystal reference frame. Crystal orientations can then be described by the Euler angles between the fixed and crystal reference frames as shown in Fig. 2. The Euler angles are defined by a positive (right-hand rule) rotation of θ about the y-axis, followed by a positive rotation of ϕ about the z_c-axis.

5.1 Cubical Solid Subjected to Uniaxial Extension. The finite element mesh has 375 hexahedral elements and is shown in Fig. 3. The solid has a square cross section with an area of 1×1 m^2, a height of 3 m, and is fixed to rigid caps at its top and bottom ends. The bottom cap is fixed to the support while the top cap is pulled vertically by an amount $\delta = \delta(t)$. The kinematics of deformation is such that the top cap remains horizontal but can translate in the lateral direction. Conventional isotropic plasticity models, such as the J_2 plasticity model, would predict that the top cap will simply move vertically upwards with no horizontal translation relative to the bottom end. However, with the anisotropy produced by crystal plasticity, we show below that in addition to a vertical extension the solid will also displace horizontally by an amount that depends on crystal orientation.

We assume the following properties of the crystal: $E = 15$ GPa, $\nu = 0.37$, $\tau_{Y0} = 20$ MPa, and $h = 0$. We consider three crystal orientations as shown in Table 1. Figure 4 shows the relative positions of the top end of the solid (cross-section with a mesh) relative to the fixed bottom end (cross section without a mesh) after stretching the solid at 1% vertical strain ($\delta = 3$ cm) for the three crystal orientations. The lateral displacement of the top end of the solid varies with crystal orientation, with the most pronounced lateral movement exhibited at orientation 1.

Figure 5 shows a more revealing deformation pattern for the solid at crystal orientation 1. As the solid is stretched, a deformation band forms on a plane that is not aligned with any of the fixed coordinate planes. We remark that the finite element mesh used in this study has no imperfection whatsoever. The band formed in the solid is purely a result of plastic slips on the most favorably oriented glide planes in the crystal. These results suggest that the propensity of a crystalline solid to undergo strain localization in the form of a deformation band depends on the orientation of the crystal lattice relative to loading direction.

Table 2 Cubical solid under uniaxial extension: convergence profile of newton iterations. Tabulated errors at different crystal orientations are based on the relative norm of residual force vector $\|\boldsymbol{r}^k\|/\|\boldsymbol{r}^0\|$.

Verticalstrain	Iteration	Orientation 1	Orientation 2	Orientation 3
0.5%	1	1.00e + 00	1.00e + 00	1.00e + 00
	2	8.24e − 16	6.38e − 16	3.37e − 12
1.0%	1	1.00e + 00	1.00e + 00	1.00e + 00
	2	7.56e − 16	6.56e − 16	7.35e − 16
1.5%	1	1.00e + 00	1.00e + 00	1.00e + 00
	2	5.80e − 11	6.84e − 16	6.75e − 16

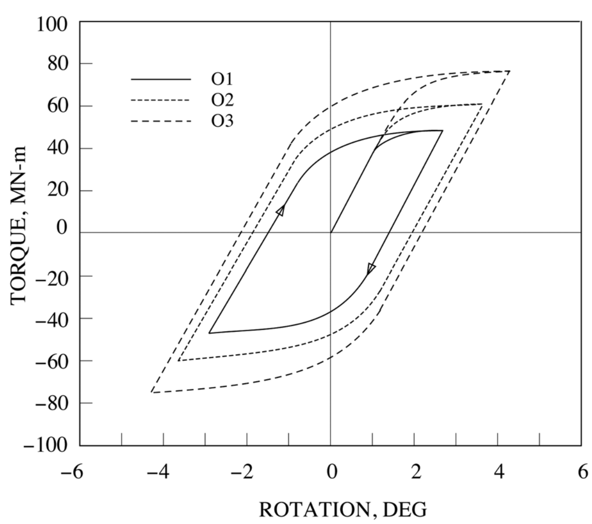

Fig. 7 Cyclic torsion versus angular twist for cylindrical solid at crystal orientations O1, O2, and O3

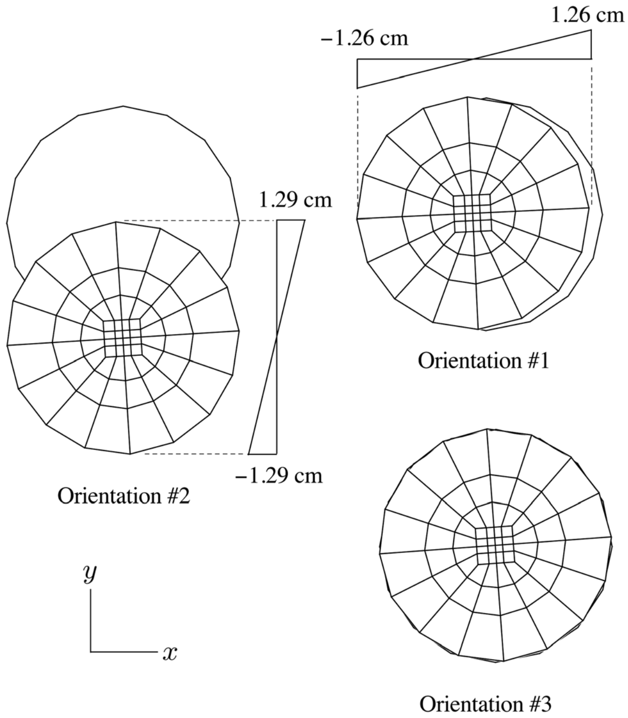

Fig. 8 Lateral and vertical movement of top end (cross-section with a mesh) relative to bottom end (cross-section without a mesh) at different crystal orientations. Lateral displacements magnified 80 ×. Crystal orientation 3 produced pure twisting with no rocking.

Table 3 Cylindrical solid under cyclic torsion: convergence profile of newton iterations. Tabulated errors at different crystal orientations are based on the relative norm of residual force vector $\|\boldsymbol{r}^k\|/\|\boldsymbol{r}^0\|$.

Torque	Iteration	Orientation 1	Orientation 2	Orientation 3
$T_{\max}$	1	1.00e + 00	1.00e + 00	1.00e + 00
	2	6.30e − 01	6.63e − 01	6.21e − 01
	3	5.98e − 09	1.00e − 08	3.60e − 01
	4	—	9.85e − 09	5.62e − 09
0	1	1.00e + 00	1.00e + 00	1.00e + 00
	2	1.28e − 09	1.28e − 09	1.38e − 09
$-T_{\max}$	1	1.00e + 00	1.00e + 00	1.00e + 00
	2	6.10e − 01	5.60e − 01	6.86e − 01
	3	8.65e − 04	9.12e − 09	5.23e − 09
	4	2.36e − 05	—	—
	5	6.44e − 07		
	6	6.12e − 09		
0	1	1.00e + 00	1.00e + 00	1.00e + 00
	2	1.28e − 09	1.32e − 09	1.82e − 09

Table 2 shows the convergence profiles of global Newton iterations expressed in terms of the ratio of the relative norm of the global residual force vector. With very few exceptions (not shown in this table), the global iterations needed no more than two iterations to achieve convergence to machine precision. As noted earlier, the problem becomes a linear one as soon as the active slips are identified, and in this example it took two iterations to identify these active slip systems.

5.2 Cylindrical Solid Subjected to Cyclic Twisting. In this example, we apply one full cycle of torsion on a cylindrical solid, modeled with 640 hexahedral finite elements shown in Fig. 6. The solid is fixed at the bottom, and the top is attached to a rigid cap on which two horizontal eccentric forces equal in magnitude but opposite in direction are applied. The rigidity of the cap prevents the top surface from warping but does not inhibit it from translating in any direction. As in the previous example, we test three different crystal orientations summarized in Table 1. The crystals are assumed to have the same material parameters as in the previous example.

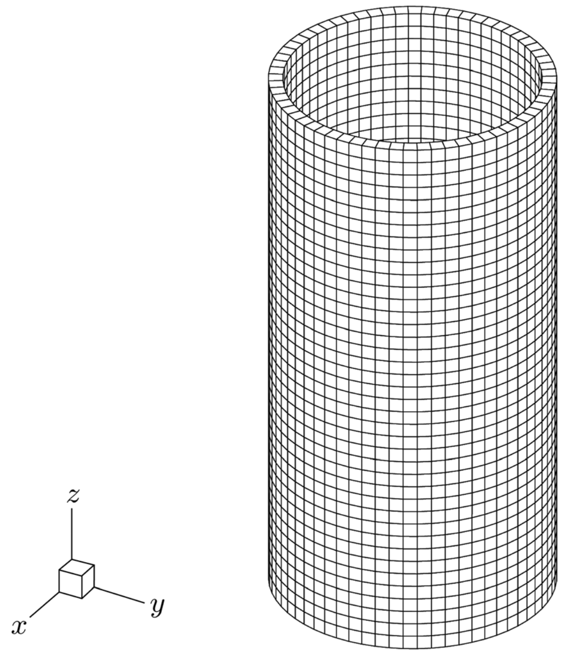

Fig. 9 Finite element mesh for a hollow cylinder subjected to torsional twisting. The cylinder has a height of 4 m, outer diameter of 2 m, and thickness of 0.1 m. The mesh has 5148 nodes and 2560 eight-node hexahedral elements, all integrated with the *B*-bar option.

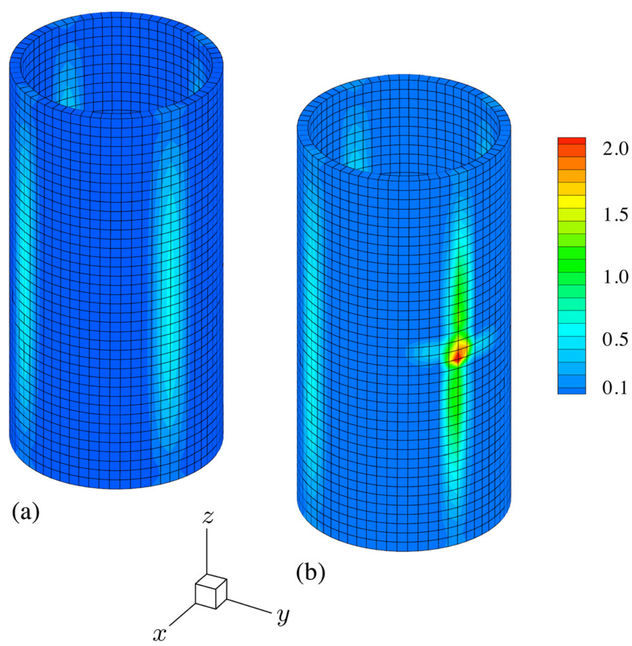

Fig. 10 Deformation bands forming in the hollow cylinder subjected to torsional twisting: (*a*) uniform crystal orientation 3 and (*b*) crystal orientation 3 with an imperfection in the form of crystal orientation 1 in four adjacent elements. Color bar is second invariant of deviatoric plastic strain in percent.

Table 4 Twisting of a hollow cylinder: convergence profile of newton iterations. Tabulated errors at different crystal orientations are based on the relative norm of residual force vector $\|r^k\|/\|r^0\|$.

Percent twist	Iteration	Uniform	Non-uniform
50%	1	1.00e + 00	1.00e + 00
	2	2.29e − 15	2.13e − 10
	3	—	3.08e − 16
100%	1	1.00e + 00	1.00e + 00
	2	9.64e − 09	1.13e − 07
	3	3.20e − 16	6.73e − 08
	4	—	5.01e − 09
	5		2.82e − 11
	6		1.21e − 12
	7		2.95e − 16

Figure 7 shows the hysteretic torque-rotation curves generated for the three crystal orientations. The torque was increased to its maximum value so that the structure would yield everywhere. The limit load was then determined from the last convergent step. We see from Fig. 7 that the ultimate loads, $\pm T_{\max}$, vary with crystal orientation and is highest for orientation 3, where the crystal axes are aligned to the coordinate axes. All hysteretic loops close, as to be expected from an elastic-perfectly plastic constitutive response.

Figure 8 shows the lateral and vertical movements of the top end of the solid when the torque reaches the value $T_{\max}$ during the initial part of loading. We see that for crystal orientations 1 and 2, the top end of the cylinder translated laterally and vertically relative to the fixed bottom base in such as way as to define a rocking mode. This is because for these two orientations, the crystal slip directions are not aligned with the direction of twisting. In contrast, no rocking mode can be seen for crystal orientation 3, where the crystal axes are aligned with the coordinate axes and, hence, with the sense of twisting.

Table 3 summarizes the convergence profiles of Newton iterations at various stages of loading. All iterations below the limit loads are superconvergent, i.e., the errors dropped immediately to zero once the active systems have been found, with the exception of the load steps near the limit loads designated as $\pm T_{\max}$ in this table. We recall that load steps near the limit load are most difficult to converge because they are close to the plateau of the torque-twist curve where the slope is flat and where the load cannot be increased further. This is exemplified by the convergence rate at $-T_{\max}$ for orientation 1, which is not quadratic. This is not a shortcoming of the iterative algorithm, but rather, it simply reflects the proximity of the solution to a physically unstable state.

5.3 Twisting of a Hollow Cylinder. As a final example, we consider a hollow cylinder shown in Fig. 9. The cylinder is clamped at both its top and bottom ends while the inner and outer vertical faces are assumed to be traction-free. The top end is then twisted while holding the bottom end fixed. Crystal orientation 3 is assumed for the cylinder, with Young's modulus $E = 15$ GPa, Poisson's ratio $\nu = 0.37$, initial yield strength $\tau_{Y0} = 10$ MPa, and hardening parameter $h = -1$ MPa (softening). Figure 10 shows the resulting plastic strain contour after subjecting the cylinder to a final torsional twist of $\theta = 1$ deg. We see four vertical deformation bands emerging from the imposed deformation. These bands did not form randomly, but rather, they are determined from the lattice orientation relative to direction of twisting. In a second simulation, a small imperfection is embedded in the cylinder by rotating the same crystal in four adjacent finite elements to orientation 1. The imperfection generates more intense localized deformation and a complementary deformation band propagating away from the imperfection.

Table 4 shows the convergence profile of Newton iterations at 50% and 100% of the total angle of twist. Observe that the iteration of the solution is superconvergent for the case where the crystal is uniformly oriented, but the introduction of the imperfection causes the iteration to slow down a little bit. The latter may be attributed to difficulty in identifying the active slip systems in the neighborhood of the imperfection. However, Newton's method still converged to machine precision after a few more iterations.

6 Summary and Conclusions

The ultimate algorithm for rate-independent crystal plasticity has been implemented into a nonlinear finite element code for analyzing the elasto-plastic deformation of 3D solids with polycrystalline microstructures. Previous work has focused only on the performance of the algorithm on the local stress-point level calculations. The present work suggests that the algorithm performs equally well in the finite element simulations of the elasto-plastic deformation of polycrystalline solids. The algorithm possesses the following attributes that make it desirable to use in a finite element code: (a) it is locally exact for incremental strain applied as a ramp function, (b) it is unconditionally convergent on the local level since it does not perform a local iteration, and (c) it is as stable as the widely used radial return algorithm for J_2 plasticity when implemented globally in a finite element code. In addition, the global Newton iteration exhibits an optimal convergence rate that is better than quadratic in some cases, implying that this iterative technique is just as effective for identifying the active constraints in polycrystalline solids as it is for solving regular nonlinear problems.

Acknowledgment

This work is supported by the US Department of Energy Grant No. DE-FG02-03ER15454 to Stanford University.

References

[1] Nikolic, R. R., and Rice, J. R., 1988, "Dynamic Growth of Anti-Plane Shear Cracks in Ideally Plastic Crystals," Mech. Mater., **7**, pp. 163–173.
[2] Rice, J. R., 1987, "Tensile Crack Tip Fields in Elastic-Ideally Plastic Crystals," Mech. Mater., **6**, pp. 317–335.
[3] Rice, J. R., and Rosengren, G. F., 1968, "Plane Strain Deformation Near a Crack Tip in a Power-Law Hardening Material," J. Mech. Phys. Solids, **16**, pp. 1–12.
[4] Mandel, J., 1965, "Generalisation de la theorie de la plasticite de W.T. Koiter," Int. J. Solids Struct., **1**, pp. 273–295.
[5] Hill, R., 1966, "Generalized Constitutive Relations for Incremental Deformation of Metal Crystals by Multislip," J. Mech. Phys. Solids, **14**, pp. 95–102.
[6] Maier, G. A., 1970, "Matrix Structural Theory of Piecewise Linear Elastoplasticity With Interacting Yield Planes," Meccanica, **5**, pp. 54–66.
[7] Rice, J. R., 1971, "Inelastic Constitutive Relations for Solids: An Internal Variable Theory and its Application to Metal Plasticity," J. Mech. Phys. Solids, **19**, pp. 433–455.
[8] Hill, R., and Rice, J. R., 1972, "Constitutive Analysis of Elastic-Plastic Crystals at Arbitrary Strain," J. Mech. Phys. Solids, **20**, pp. 401–413.
[9] Asaro, R. J., and Rice, J. R., 1977, "Strain Localization in Ductile Single Crystals," J. Mech. Phys. Solids, **25**, pp. 309–338.
[10] Bishop, J. F. W., and Hill, R. A., 1951, "A Theory of the Plastic Distortion of a Polycrystal Aggregate Under Combined Stresses," Philos. Mag., **42**, pp. 414–427.
[11] Bishop, J. F. W., and Hill, R., 1941, "A Theoretical Derivation of the Plastic Properties of Polycrystalline Face-Centered Metal," Philos. Mag., **42**, pp. 1298–1307.
[12] Lin, T. H., 1957, "Analysis of Elastic and Plastic Strains of a Face-Centered Cubic Crystal," J. Mech. Phys. Solids, **5**, pp. 143–149.
[13] Hutchinson, J. W., 1970, "Elastic-Plastic Behavior of Polycrystalline Metals and Composites," Proc. R. Soc. London, Ser. A, **319**, pp. 247–272.
[14] Budiansky, B., and Wu, T. T., 1962, "Theoretical Prediction of Plastic Strains of Polycrystals," *Proceedings of the Fourth U.S. National Congress on Applied Mechanics*, R. M. Rosenberg, ed., ASME, New York, pp. 1175–1185.
[15] Iwakuma, T., and Nemat-Nasser, S., 1984, "Finite Elastic-Plastic Deformation of Polycrystalline Metals," Proc. R. Soc. London, Ser. A, **394**, pp. 87–119.
[16] Peirce, D., Asaro, R. J., and Needleman, A., 1982, "An Analysis of Uniform and Localized Deformation in Ductile Single Crystals," Acta Metall., **30**, pp. 1087–1119.
[17] Kocks, U. F., 1970, "The Relation Between Polycrystal Deformation and Single-Crystal Deformation," Metall. Trans., **1**, pp. 1121–1143.
[18] Kocks, U. F., and Canova, G. R., 1981, "How Many Slip Systems, and Which?," *Deformation of Poly-Crystals: Mechanisms and Microstructures, Proceedings 2nd Riso International Symposium on Metallurgy and Materials Science*, N. Hansen, A. Horsewell, T. Leffers, and H. Liholt, eds., Riso National Laboratory, Roskilde, Denmark, pp. 35–44.

[19] Havner, K. S., 1982, "Minimum Plastic Work Selects the Highest Symmetry Deformation in Axially Loaded f.c.c. Crystals," Mech. Mater., **1**, pp. 97–111.
[20] Koiter, W. T., 1957, "Stress-Strain Relations, Uniqueness and Variational Theorems for Elastic-Plastic Materials With a Singular Yield Surface," Q. Appl. Math., **11**, pp. 350–354.
[21] Simo, J. C., Kennedy, J. G., and Govindjee, S., 1988, "Non-Smooth Multisurface Plasticity and Viscoplasticity: Loading/Unloading Conditions and Numerical Algorithms," Int. J. Numer. Methods Eng., **26**, pp. 2161–2185.
[22] Borja, R. I., and Wren, J. R., 1993, "Discrete Micromechanics of Elastoplastic Crystals," Int. J. Numer. Methods Eng., **36**, pp. 3815–3840.
[23] Cuitiño, A. M., and Ortiz, M., 1992, "Computational Modelling of Single Crystals," Modell. Simul. Mater. Sci. Eng., **1**, pp. 225–263.
[24] Steinmann, P., and Stein, E., 1996, "On the Numerical Treatment and Analysis of Finite Deformation Ductile Single Crystal Plasticity," Comput. Methods Appl. Mech. Eng., **129**, pp. 235–254.
[25] Nemat-Nasser, S., and Obata, M., 1986, "Rate-Dependent Finite Elastic-Plastic Deformation of Polycrystals," Proc. R. Soc. London, Ser. A, **407**, pp. 343–375.
[26] Pan, J., and Rice, J. R., 1983, "Rate Sensitivity of Plastic Flow and Implications for Yield Surface Vertices," Int. J. Solids Struct., **19**, pp. 973–987.
[27] Dumoulin, S., Hopperstad, O. S., and Berstad, T., 2009, "Investigation of Integration Algorithms for Rate-Dependent Crystal Plasticity Using Explicit Finite Element Codes," Comput. Mater. Sci., **46**, pp. 785–799.
[28] Ling, X., Horstemeyer, M. F., and Potirniche, G. P., 2005, "On the Numerical Implementation of 3D Rate-Dependent Single Crystal Plasticity Formulations," Int. J. Numer. Methods Eng., **63**, pp. 548–568.
[29] Anand, L., and Kothari, M. A., 1996, "Computational Procedure for Rate-Independent Crystal Plasticity," J. Mech. Phys. Solids, **44**, pp. 525–558.
[30] Schröder, J., and Miehe, C., 1997, "Aspects of Computational Rate-Independent Crystal Plasticity," Comput. Mater. Sci., **9**, pp. 168–176.
[31] Miehe, C., and Schröder, J. A., 2001, "Comparative Study of Stress Update Algorithms for Rate-Independent and Rate-Dependent Crystal Plasticity," Int. J. Numer. Methods Eng., **50**, pp. 273–298.
[32] Busso, E., and Cailletaud, G., 2005, "On the Selection of Active Slip Systems in Crystal Plasticity," Int. J. Plast., **21**, pp. 2212–2231.
[33] Wilkins, M. L., 1964, "Calculation of Elastic-Plastic Flow," *Methods of Computational Physics*, Vol. 3, B. Alder, ed., Academic Press, New York.
[34] Borja, R. I., 2012, *Plasticity Modeling and Computation*, Springer-Verlag, Berlin, in press.
[35] Borja, R. I., 2008, "Assumed Enhanced Strain and the Extended Finite Element Methods: A Unification of Concepts," Comput, Methods Appl. Mech. Eng., **197**, pp. 2789–2803.
[36] Borja, R. I., and Regueiro, R. A., 2001, "Strain Localization of Frictional Materials Exhibiting Displacement Jumps," Comput. Methods Appl. Mech. Eng., **190**, pp. 2555–2580.
[37] Borja, R. I., 2000, "A Finite Element Model for Strain Localization Analysis of Strongly Discontinuous Fields Based on Standard Galerkin Approximations," Comput. Methods Appl. Mech. Eng., **190**, pp. 1529–1549.
[38] Taylor, G. I., 1938, "Plastic Strain in Metals," J. Inst. Met., **62**, pp. 307–324.
[39] Nowinski, J. L., 1981, *Applications of Functional Analysis in Engineering*, Plenum Press, New York.